BME SENIOR CAPSTONE PROJECT

Strydr

Kenneth A. Meyerson, Class of 2020

Mark Cronin-Golomb (Adviser)

Abstract: Strydr is a proof-of-concept lower-limb exoskeleton device implementing the StryDrive, a balanced cycloidal actuator powered with brushless motors. The objective of Strydr is to provide strength augmentation and motion control for medical and industrial applications. Two key components, the StydSense DSP enhanced surface EMG control and the StrydLight carbon-fiber composite structural frame elements, were codeveloped to provide a complete experience for design testing. Development of the project was accelerated through iterative design, rapid prototyping, and qualitative testing. COVID-19 related closures of laboratories and manufacturing facilities, suspended system development and limited quantitative testing. Continued research and development are therefore required.

Keywords: Exoskeleton, Actuator, Cycloidal Reducer, Electromyogram Control, Composites

ELEMENTS OF ENGINEERING DESIGN

Objectives of the Project: The goal for Strydr is to develop a proof of concept lower limb exoskeleton that can aid with strength and motion control through the application of the novel, StyrDrive actuator.

Components Designed: Strydr features three subsystems: StryDrive, StrydSense, and StrydLight.

- **StryDrive** is a parameterized and iteratively designed balanced cycloidal reduction gearbox. I developed a tolerance compensation protocol for in-house fabrication to minimize errors introduced during prototype fabrication. Note: A thermal camera was intended to be used to measure heat generated by the gearbox and motor during testing, but this has not yet been possible due to manifesting and testing delays.
- **StrydSense** complements the StyrDrive, which includes an analogue front end surface electromyogram and embedded digital signal processing routine. Signal processing is executed locally using hardware accelerated digital signal processing on an Arm Cortex-M4 processor. An AC Power line and 4-band BiQuad equalizer were designed in MATLAB and implemented with hardware accelerated functions on an ARM Cortex-M4 processor. Furthermore, I developed and refined a script to transform and format MATLAB Second-Order Sections (SOS) coefficients for IIR BiQuad filters into C header files.
- **StrydLight** is a carbon fiber frame used as the primary structural element in the telescoping frame that accommodates varying heights and weights of individuals for ease of use. Magnetic aligned straps are used to quickly and easily secure to the body, along with a load bearing ankle joint with two degrees of freedom. A 2-degree-of-freedom, load-bearing ankle joint transfers the weight and loading of the exoskeleton directly into the ground.

Scientific, math, and/or engineering methods applied: Mechanical engineering principles including structural analysis, machine design, drafting, and fabrication were used to aid in the design of the StryDrive and StrydLight systems. The design of joints and frames applied principals of physiology. Electrical engineering principles and circuit board design were applied to the design and fabrication of discrete components in StryDrive and StrydSense. Principals of electrophysiology guided the design of the StrydSense control system. Computer science was applied in the choice of embedded system architecture, the development of digital filters, and the hardware accelerated software design.

Tests and the quantitative milestones: Iterative design and testing were applied throughout the development process of Strydr.

- StryDrive was iterated over five prototype generations before the final cycloidal design was specified. Characterization of the actuator through static and cyclic loading tests were suspended due to manufacturing and testing delays introduced by COVID-19.
- Behavior of the core signal acquisition and processing techniques developed in StrydSense was verified with quantitative comparison using remote processing performed in MATLAB. Implementation and testing of simultaneous sampling and processing, zero-phase filtering, and control signal ramping were suspended due to COVID-19.
- StrydLight was developed over two generations of iterative design and qualitative testing and yielded a minimally viable frame, ankle, and body interface design. The implementation and testing of all scheduled features have not yet been completed due to COVID-19,

Realistic constraints considered: A fully featured lower-limb exoskeleton with layered redundancy and safety features is beyond the scope possible in a single academic year of development funded exclusively by a single author. Hardware and software deliverables are minimally viable, proof-of-concept platforms for future research.

- Cycloidal reducers are unstandardized and part design is always custom. Comprehensive parameterization of the gearbox design to assess material stress and mechanical efficiency are beyond the scope of this project.
- The author’s earlier experience in digital filter design did not include design transfer to embedded solutions or implementation with hardware accelerated functions.
- The author’s earlier experience in embedded solutions did not include ARM Cortex-M4 embedded processors and the implied system bus topology, embedded firmware development environment, and hardware accelerated functions abstraction layer.
- Substitution of certified carbon-fiber structural elements with hobby grade carbon-fiber materials reduced proof-of-concept development cost and may not perform to the same standards.

Alternative solutions considered:

- Motor choice involved the consideration of four motor families (Brushed, Servo, Stepper, Brushless). Brushed and servo motors rely on mechanical commutation that generates mechanical wear over time and electrical arcs under large loads.
- Gearbox choice involved the consideration of planetary, hypoid, and cycloidal gears. The standardized designs provided by planetary and hypoid gears would have minimized the time investment into gearbox parameterization, however they would not have offered the acoustic, loading, and backlash benefits of the cycloidal drive.
- Exoskeleton controls are specific to the application. Maximizing the utility offered by exoskeletons without detracting from the ease of use requires intuitive controls that do not require direct interaction. I could use button-based and lean-based control methods proven in research and commercial designs as practical alternatives to EMG control.

Project Summary: Strydr was partially successful in the ambitious design and testing of the StryDrive, StrydSense, and StrydLight subsystems.

- The parameterization and design of an in-joint, balanced cycloidal actuator was a success. Manufacturing and quantitative characterization of the cycloidal reducer through static and cyclic loading tests are incomplete due to COVID-19 and will not occur prior to the final submission of the project.
- The design and implementation of core signal acquisition and hardware accelerated processing techniques required for SEMG controls was a success. However, implementation and testing of simultaneous sampling and processing, zero-phase filtering, and control signal ramping are incomplete due to COVID-19 and will not occur prior to the final submission of this project.
- The telescoping frame, user interface, and passive ankle design were completed. The design refinement and testing of passive return to center behavior of the ankle joint, shoe platform, and tool-free telescoping handle are incomplete due to COVID-19 and will not occur prior to the final submission of this project.

DESIGN FLOW CHARTS

Current stage of development marked purple

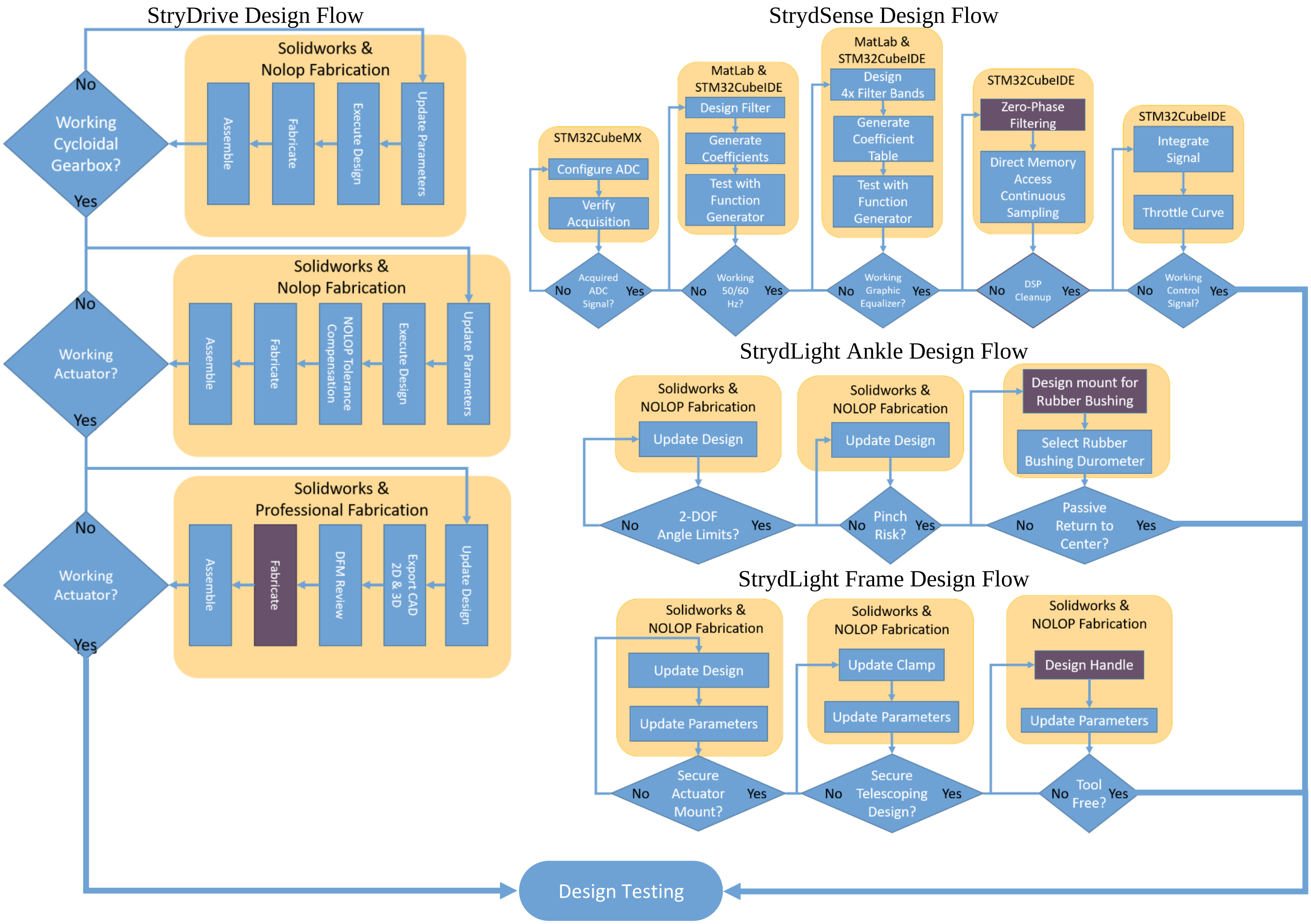

INTRODUCTION

Exoskeletons augment human capabilities and performance in specific tasks. Unlike prosthesis, the main objective is to increase the power of the user by mirroring their motion and providing assistance on demand. Exoskeletons are appealing where the presence of a human operator is both preferred and critical. Popular applications target the mobility challenges of elderly and spinal cord injury patients as well as promoting stroke recovery through rehabilitiation. Styrdr features three specific aims delivered as three systems which each include two primary design components. Strydr differs from existing solutions and research because of its brushless motor implementation and balanced cycloidal gearbox.

The visions of early exoskeletons and modern-day solutions share a desire to augment the capabilities of the human body. The potential applications for this augmentation technology are only limited by the necessity of a human operator. Many exoskeleton designs adhere to the patented visions of Nicholas Yagn in the 1890s (US420179, US44684). These simple and fantastic designs sought to improve walking, jumping, and running. Although the idea of storing energy in loaded springs and pressurized gas seems primitive, exoskeletons are consistently limited by available technology. Recent advances in energy storage, torque generation, and material science have inspired new possibilities for exoskeleton design.

The first contemporary exoskeleton design was commissioned by the US Army/Navy in the early 1960s to design and assemble the *Hardiman* exoskeleton to imbue its user with the strength to lift 680kg. The system was limited by the servo, sensor, and mechanical technology available at the time, but its development led to the formation two core design principles:

1. The recreation of all human motion is impractical from an engineering standpoint.
2. Only specific human motions should be duplicated and must be determined experimentally. (Mosher, 1967)

Exoskeletons have since been developed into several experimental and commercialized solutions. Lower Limb Exoskeleton (LLE) solutions for medical professionals, industrial workers, and military personnel are pursued by independent researchers, private enterprises, and government contractors (Bogue, 2015).

The audience for this industry potentially includes the entirety of the human population. Research into the potential benefits and applications of exoskeleton devices for rehabilitative treatments have defined the growth of this field. Therapeutic and rehabilitative applications for older adults and stroke patients are two unique directions within the industry.:

Approximately 10% of adults between their sixties and seventies develop a gait disorder which balloons to excess of 60% of adults older than 80 (Pirker & Katzenschlager, 2017). The structural support and enhanced motion control help overcome age-related mobility challenges such as achieving sufficient foot clearance over obstacles.

Stroke patients, depending on the severity of their injury, may require months to years of training to regain muscular control. Per annum, there are 191,000 new patients in Japan, 795,000 new patients in United States, and 200,000,000 new patients in China (Zhang et al., 2017). Although parallel limb exoskeletons are primarily strength augmentation devices, they can also supply resistance to motion for training and rehabilitation.

Additional applications include restoring mobility independence for individuals affected by paraplegia. Within the United States, approximately 288,000 individuals struggle with personal mobility with an addition 17,700 new patients per year. The lifetime costs for individuals injured between the ages of 25 and 50 are estimated to be more than one million dollars (*Spinal Cord Injury Facts and Figures at a Glance*, 2017).

Industrial applications of exoskeleton devices may also be considered preventative healthcare applications. Although 70% of workplace injuries are unreported within the United States (Fagan & Hodgson, 2017), approximately 65% of the 2.8 million reported, non-lethal injuries in the combined private and retail sectors are associated with overexertion. 30.7% and 38.4% of reported injuries are associated with sprains/strains/tears and 15.9% and 16.1% are associated soreness/pain (Bureau of Labor Statistics, 2019). Exoskeletons have shown promise in alleviating over exertion in light lifting tasks (Masood et al., 2016).

However, studies pursuant of tangible efficiency gains show that additional development is required. The first study of metabolic cost and gait impact associated with an LLE in 2010 found that the LLE increased the difficulty of the task (Gregorczyk et al., 2010).

The use of exoskeletons and other wearable robotics pose ethical and social concerns. The cost of consumer models is beyond the reach of the majority of the population and a dependency on the device is developed. Beyond the concerns affecting individuals who gain a world of independence through this technology, there is also the possibility that augmentation results in the dehumanization of manual laborers and soldiers (Greenbaum, 2016). Although the full-scale introduction of these products seems distant, the solutions in development and currently available are very real.

Popular lower-limb exoskeleton designs include the use of soft robotics and artificial muscles, spring loaded gearboxes, and Bowden cable-based systems. The advantages and limitations of these solutions are applied to specific applications to provide the best experience.

Soft exoskeletons are composed of fabrics and flexible materials and deliver torque through the users joints to minimize the exoskeletons impact on gait and motion. These solutions are light weight and are well suited for non-ambulatory treatments in a clinical setting for as stroke, spinal cord injury, and gait disorders. These designs, however, can be difficult to design and can deform uncomfortably around the user. Actuators capable of generating large lifting forces often rely on external pressure generators which make the design less practical for transport and independent mobility solutions (Sanchez-Villamañan et al., 2019).

STRYDRIVE – SUMMARY

The StryDrive actuator employs a low-profile, in-joint actuator design through the application of a closed-loop and field-oriented controlled brushless motor and the parameterization and fabrication of an in-joint, balanced cycloidal actuator. The actuator is designed for use at the hip and knee.

STRYDRIVE – GEARBOX METHODS

The absence of standardized cycloidal gearboxes design makes each application custom and unique. I developed a custom design for cycloidal gears from existing literature and geometric parameterizations, and I used iterative design to refine design rules and guidelines.

The StryDrive design, with peak torque output in excess of 100 Nm, competes with marketed exoskeleton solutions according to a comparative report of contemporary rigid and compliant exoskeleton designs (Sanchez-Villamañan et al., 2019). The theoretical peak motor torque supported by the motor design is 3 [Nm], and a reduction ratio of 36:1 was selected based to provide a theoretical maximum of 108 [Nm] of torque in a perfectly efficient system (see appendix section on Brushless DC Motors for more information).

Although the gearbox ratio is 36:1, the actuator is rotationally limited to 135 degrees of motion. This range of motion is inclusive of the range motion for hip and knee flexion in the sagittal plane for men between the ages of 9 and 19 in peak condition (Soucie et al., 2011). The motor requires 12.5 revolutions to rotate the full degrees of motion.

There are many derivations used to derive cycloidal gears varying in degrees of complexity. I reviewed and experimented with several approaches with varying degrees of success and derived a method based on a modified epitrochoid curve that I could fully understand. The basic parameters are as follows:

Name	Symbol	Expression or Requirements	Notes
Gear Tooth Count	N_{Gear}		Integer Value
Ring Tooth Count	N_{Ring}	$N_{Ring} = N_{Gear} + 1$	Integer Value
Reduction Ratio	i	$i = \frac{N_{Gear}}{N_{Gear} - N_{Ring}}$	Integer Value
Ring Diameter	D		Measurement (mm)
Ring Tooth Diameter	d	Must satisfy: $d \leq D sin\left(\frac{\pi}{N_{Ring}}\right)$	Measurement (mm)
Eccentricity	e	Must satisfy: $e < \left(\frac{d}{2}\right)$	Measurement (mm)

Table 1. The primary parameters that affect the design of the gearbox.

The ring is composed of N_{Ring} pins of diameter d evenly distributed about the diameter D from the origin with a spacing of $\frac{2\pi}{N_{Ring}}$. The gear geometry is defined by polar equation set below for which $0 < \theta < 2\pi$ and is changed by an inset defined by $\frac{d}{2}$.

$$x(\theta) = (R_a + R_b)\cos(\theta) + e * cos\left(\frac{R_a + R_b}{R_b}\theta\right)$$

$$y(\theta) = (R_a + R_b)\sin(\theta) + e * sin\left(\frac{R_a + R_b}{R_b}\theta\right)$$

Expressions $\begin{cases} R_a = (N_{Gear} - 1)\left(\frac{D}{2N_{Gear}}\right) \\ R_b = \frac{D}{2N_{Gear}} \end{cases}$ are derived from the relationships: $\begin{cases} R_a + R_b = \frac{D}{2} \\ \frac{R_a}{R_b} = N_{Gear} \end{cases}$

I modeled the cycloidal gear with a self-intersecting, equation driven spline in Solidworks and inset the spline by $\frac{d}{2}$ as previously described to generate the desired curve. The outer gear originally constructed static ring of cylindrical protrusions and was replaced with rolling sleeves in the final design (see STRYDRIVE – RESULTS section for relevant figures).

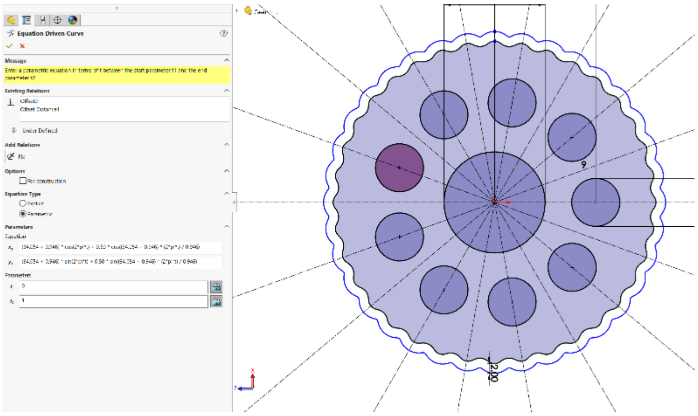

Enter a parametric equation in terms of t between the start parameter t1 and the end parameter t2

Offset0
Offset Distance1

Under Defined

☐ For construction

○ Explicit
● Parametric

x_t (34.054 + 0.946) * cos(2*pi*t) + 0.50 * cos((34.054 + 0.946) * (2*pi*t) / 0.946)
y_t (34.054 + 0.946) * sin(2*pi*t) + 0.50 * sin((34.054 + 0.946) * (2*pi*t) / 0.946)

t_1 0
t_2 1

Figure 1.a Self-Intersecting, equation-driven spline based cycloidal gear in Solidworks

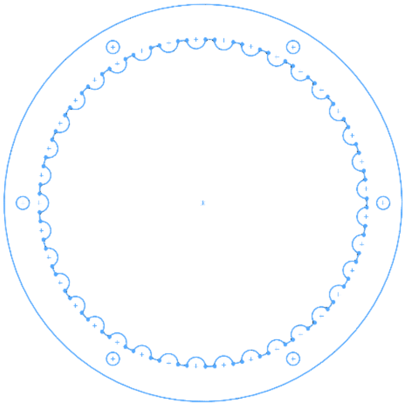

Figure 1.b Original ring design featuring static, cylindrical protrusions

I improved the gearbox design by integrating a secondary gear engaged 180 degree out of phase with the primary gear using a CAM shaft (Borislavov et al., 2012). This increases the total loading capacity of the gearbox, reduces vibrations, and further minimizes backlash.

Reduced torque is extracted from the gearbox through output shafts threaded through the body of the gears. In high torque capacity designs, these output shafts are also designed as CAM shafts in balanced designs, however the added complexity is beyond the scope of this project. I derived the number and placement of these output holes through iterative design. I found that pin holes must be evenly spaced at an arbitrary diameter and meet the following criteria:

Name	Symbol	Expression or Requirements	Notes
Number of Pins	N_{Output}	$\left(\frac{i}{N_{Output}}\right)$ must be an integer value	Integer Value
Gear 1 Position		Pins must be in line with the peaks of the tooth lobes.	
Gear 2 Position		Pins must be in line with the troughs of the tooth lobes.	

Table 2.0 Criteria for output shaft design

STRYDRIVE – MOTOR & ENCODER METHODS

I designed the StryDrive actuator around a brushless motor from an earlier project because I was familiar with its construction, configuration, and limitations. The open source oDrive controller based on the Texas Instruments DRV83xx series integrated gate driver controls the StryDrive motor. A companion STM32 microcontroller uses a field-oriented control algorithm to estimate torque, velocity, and position and instructs the gate driver to supply optimal current through the MOSFETs. I configured the startup procedure to measure the motors electrical properties to calibrate the FOC parameters but did not enable position calibration.

The brushless motor features an integrated 120-degree offset hall effect sensor array which is practical for RPM estimates for rotor position during startup, but lacks the resolution required for position control. The AS5047P Rotary Encoder was selected to be mounted on the opposite side of the gearbox (with respect to the motor and assembly midline) and modified the CAM shaft to support a OD 6mm by 2mm thick diametrically magnetized magnet. The sensor generates accurate position data when the planar separation between the encoder package and magnet is less than 2mm and central axes are aligned within the tolerance of 1.1mm (ams AG, 2016).

The IC requires a dual-sided PCB to access all of the possible interfaces. I designed and milled a single sided PCB with common SMD footprints, trace widths and vias, as reference for what sizes were possible to manufacture at Tufts and what I felt comfortable using in my design.

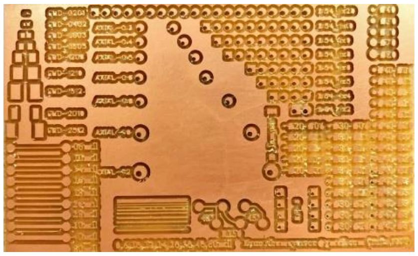

Figure 2.a Reference PCB

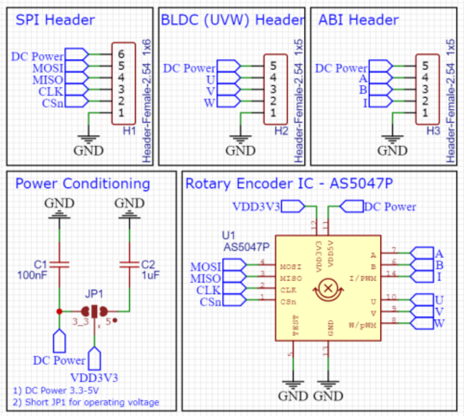

Figure 3.b Rotary Encoder Schematic

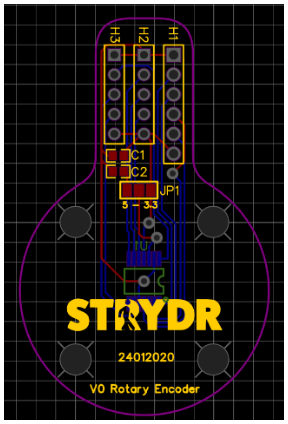

Figure 3.c Rotary encoder PCB Layout

Figure 3.d Rotary Encoder PCB Prototype

This reference guided the design and prototyping of a double-sided PCB using the Bray Bantam PCB mill based. The PCB Gerber files submitted to JLCPCB (Shenzhen JIALICHUANG Electronic Technology Development Co.,Ltd.) for fabrication. I did not order a solder paste stencil for this PCB because the order volume was small. Instead, I used the laser cutter to fabricate a single use paper stencil with the appropriate SMD footprints. Kapton tape is preferred, but the results were acceptable.

Figure 4.a Manufactured PCBs

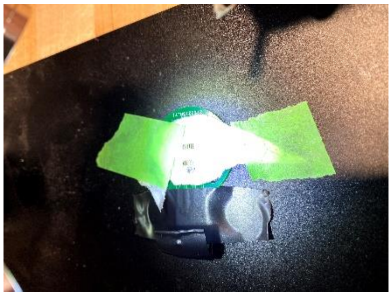

Figure 4.b Laser cut paper stencil

Figure 4.c Application of solder paste

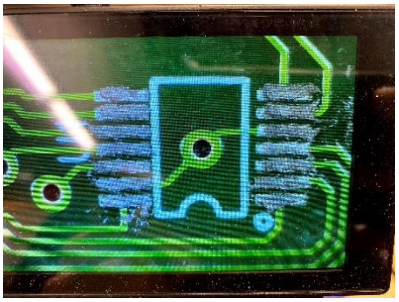

Figure 4.d Applied Solder

Figure 4.e Reflow Cycle

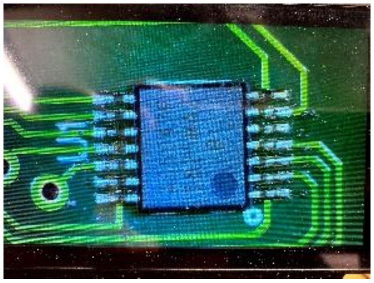

Figure 4.f Assembly Complete

A defect came to my attention when the oDrive struggled to read the rotary encoder over a range of angles. I had failed to center the encoder IC above the CAM shaft magnet. I verified this problem by testing the offset position of the rotary encoder by holding the board closer to center and reinitializing it in the oDrive software. The drift was sufficiently problematic that a revision was made, and added boards manufactured.

STRYDRIVE – RESULTS

Videos of the completed V6 assembly build using the designs demonstrate smooth and silent operation (see Figure 5). I look forward to characterizing the actuator's performance in future studies. I developed a low-cost thermal camera using the Panasonic AMG8833 IR sensor and LabVIEW's Bicubic Spline interpolation function to enhance the resolution of the chip without affecting the accuracy of the temperature data (see Figure 6). The planned testing of the StryDrive actuator involves current and temperature measurement during static and cyclic loading cycles to estimate efficiency and service life and efficiency.

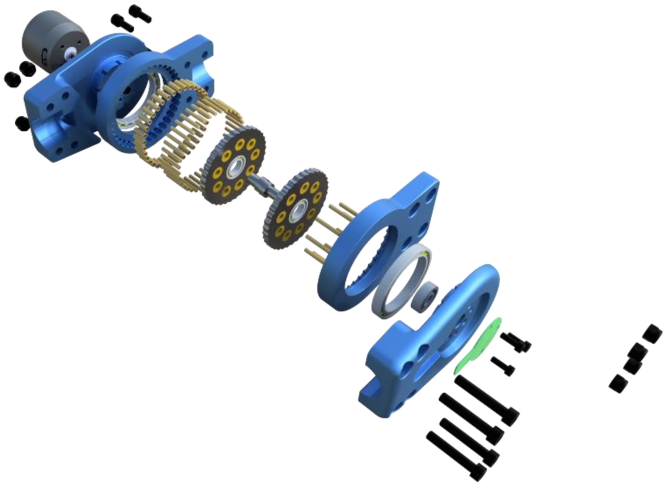

Figure 5.a
StryDrive Version 6 exploded view. Blue components are 6061-T6 aluminum, dark grey gears are JIS S45C steel, golden colored components are brass alloy, and the green component is the rotary encoder.

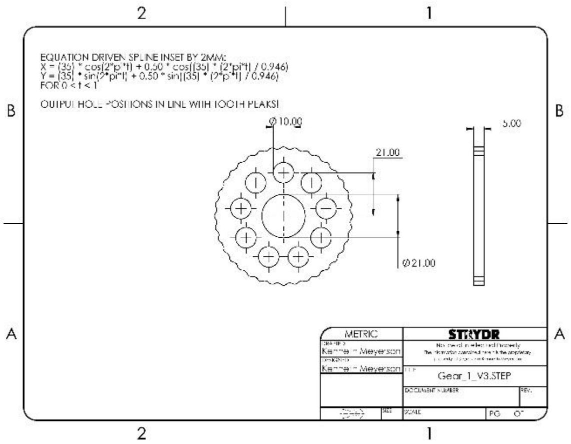

Figure 5.b Cycloidal Disk (1)

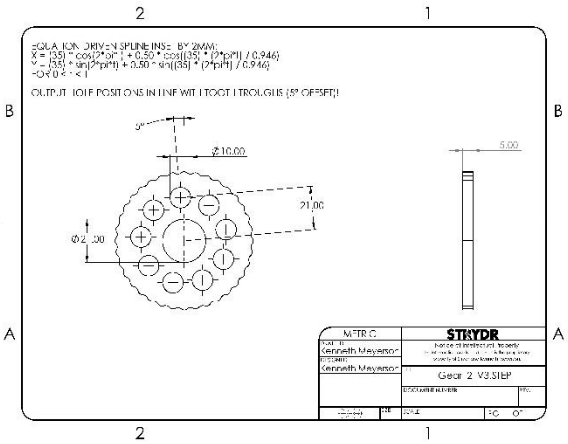

Figure 5.c Cycloidal Disk (2)

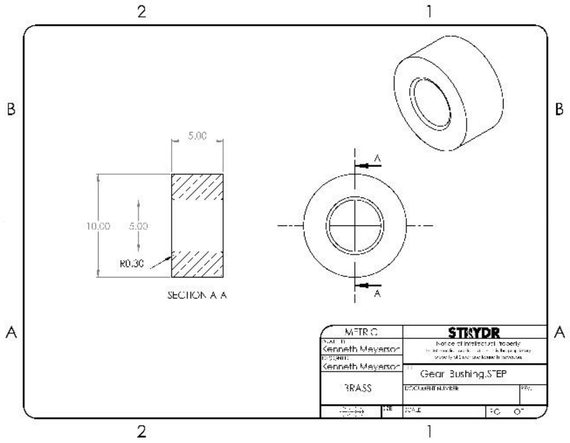

Figure 5.c Brass Alloy bushing

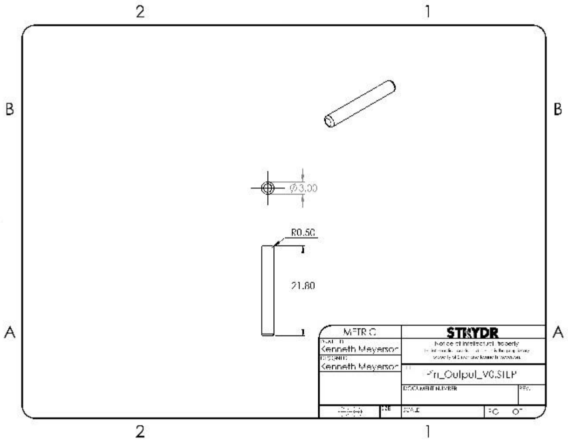

Figure 5.d Output pin

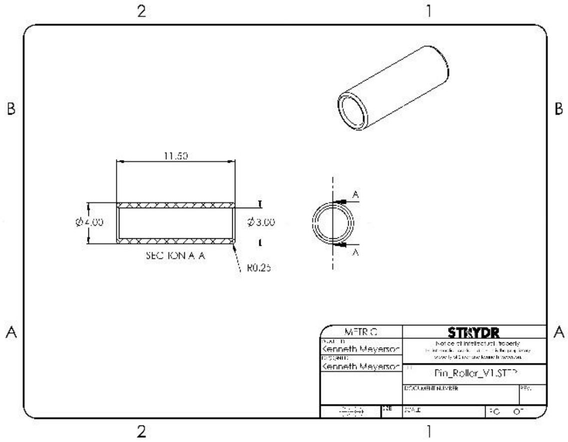

Figure 5.d Outer ring rolling sleeve

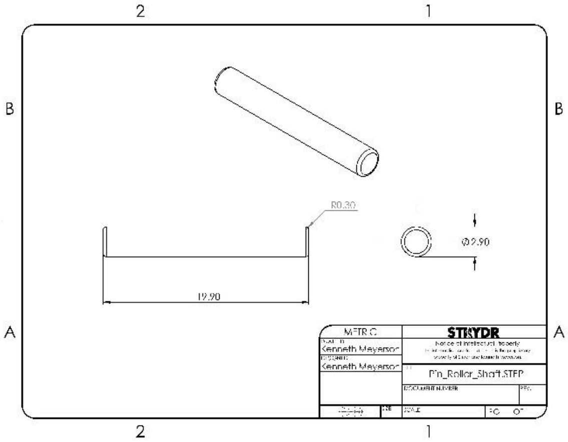

Figure 5.e Outer ring pin

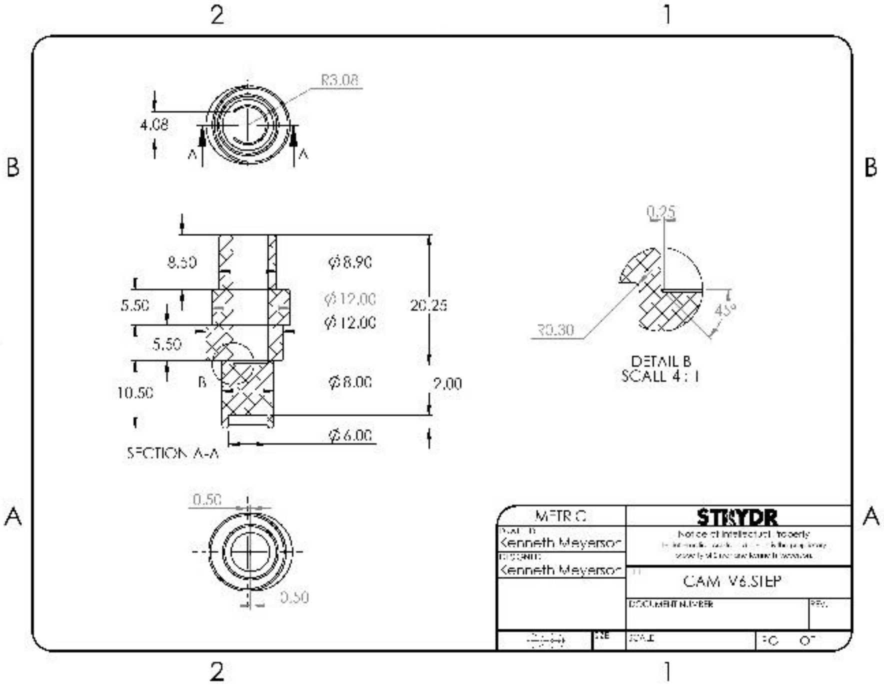

Figure 5.f CAM shaft design

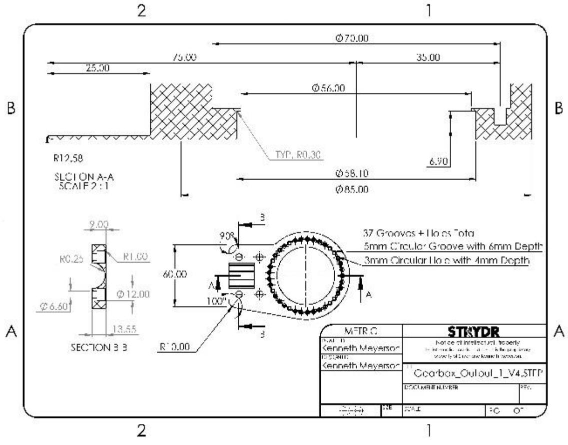

Figure 5.g Enclosure Output

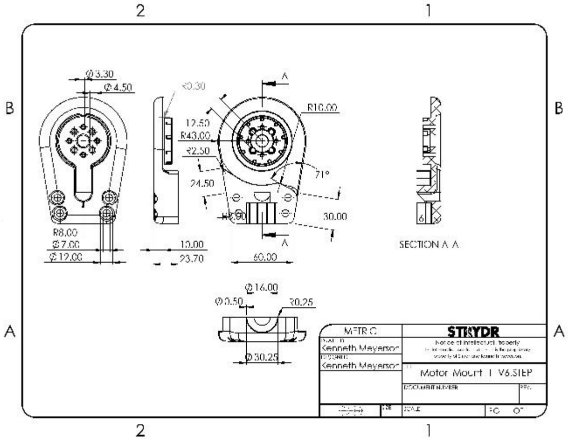

Figure 5.h Enclosure Motor Mount

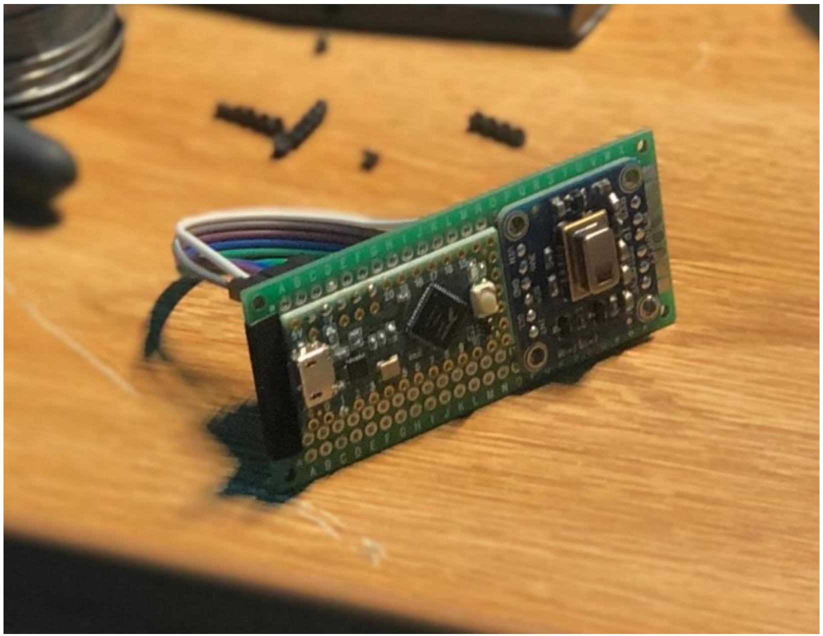

Figure 6.a
8x8 Resolution Panasonic
AMG8833
IR Thermal Camera

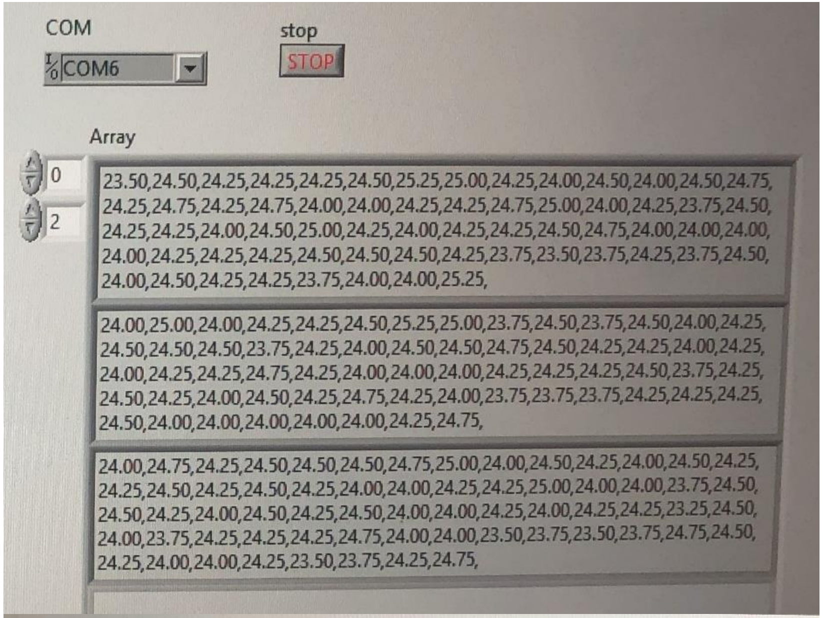

```
23.50,24.50,24.25,24.25,24.25,24.50,25.25,25.00,24.25,24.00,24.50,24.00,24.50,24.75,
24.25,24.75,24.25,24.75,24.00,24.00,24.25,24.25,24.75,25.00,24.00,24.25,23.75,24.50,
24.25,24.25,24.00,24.50,25.00,24.25,24.00,24.25,24.25,24.50,24.75,24.00,24.00,24.00,
24.00,24.25,24.25,24.25,24.50,24.50,24.50,24.25,23.75,23.50,23.75,24.25,23.75,24.50,
24.00,24.50,24.25,24.25,23.75,24.00,24.00,25.25,
```

```
24.00,25.00,24.00,24.25,24.25,24.50,25.25,25.00,23.75,24.50,23.75,24.50,24.00,24.25,
24.50,24.50,24.50,23.75,24.25,24.00,24.50,24.50,24.75,24.50,24.25,24.25,24.00,24.25,
24.00,24.25,24.25,24.75,24.25,24.00,24.00,24.00,24.25,24.25,24.25,24.50,23.75,24.25,
24.50,24.25,24.00,24.50,24.25,24.75,24.25,24.00,23.75,23.75,23.75,24.25,24.25,24.25,
24.50,24.00,24.00,24.00,24.00,24.00,24.25,24.75,
```

```
24.00,24.75,24.25,24.50,24.50,24.50,24.75,25.00,24.00,24.50,24.25,24.00,24.50,24.25,
24.25,24.50,24.25,24.50,24.25,24.00,24.00,24.25,24.25,25.00,24.00,24.00,23.75,24.50,
24.50,24.25,24.00,24.50,24.25,24.50,24.00,24.00,24.25,24.00,24.25,24.25,23.25,24.50,
24.00,23.75,24.25,24.25,24.25,24.75,24.00,24.00,23.50,23.75,23.50,23.75,24.75,24.50,
24.25,24.00,24.00,24.25,23.50,23.75,24.25,24.75,
```

Figure 6.b
Serial Data Stream
produced by Thermal
Camera Assembly

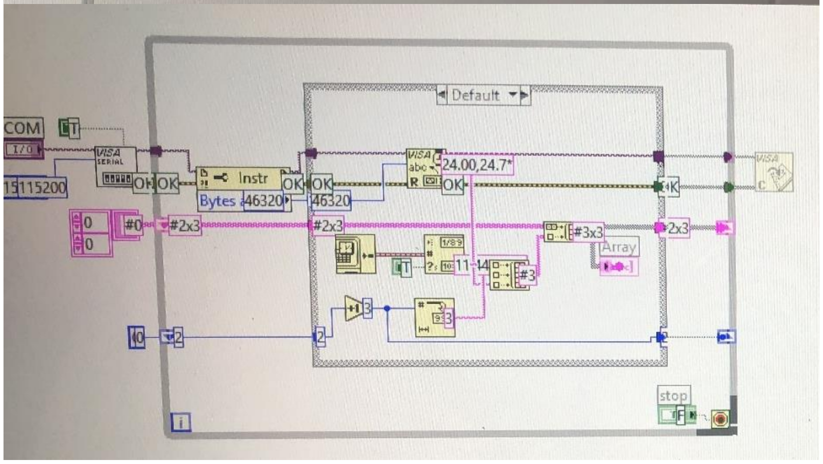

Figure 6.c
LabView Virtual
Instrument Design

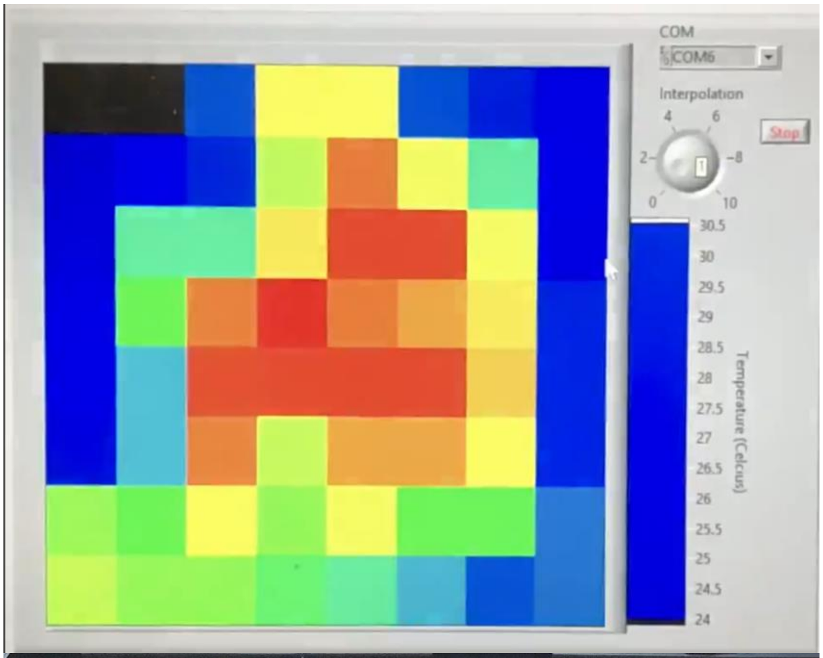
COM
COM6

Figure 6.d
Un-interpolated 8x8
Resolution IR Thermal
Camera

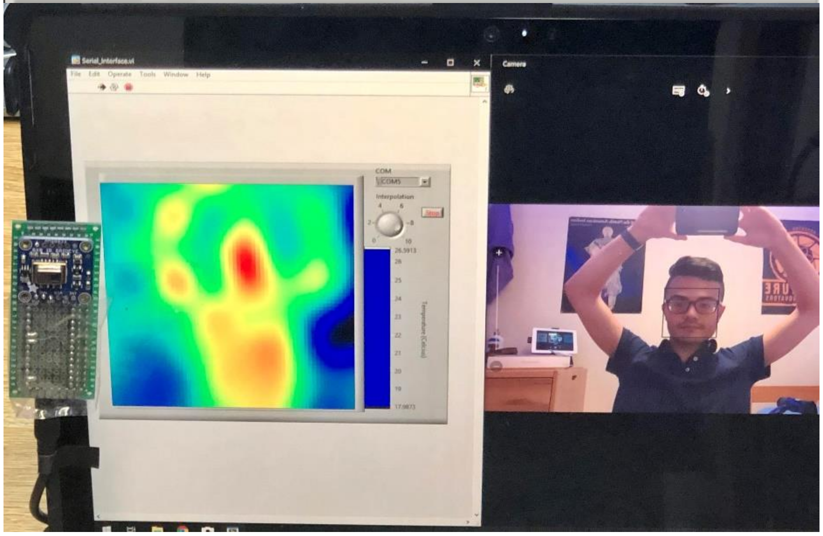

Figure 6.e
Bicubic Spline Interpolated
Panasonic AMG8833
IR Thermal Camera

GEARBOX – DISCUSSION

Solidworks Simulation and Finite Element Analysis were unable to apply the CAM mate to the surface of the cycloidal gear. This is because the gear was designed from self-intersecting equation-driven spline that produces a seam in the surface and creates a discontinuity in the surface path required for CAM motion and assembly stress simulations.

Mechanical failure of the 3D printed CAM shaft was common. I tried to produce the design with PLA, Carbon Fiber reinforced, and FormLabs durable SLA material layered in multiple directions to resolve this problem. Failure may be a symptom of the gearbox seizing and applying excess stress to the shaft, but it is also reasonable that the applied stress during normal use exceeds the shear strength of the material regardless of the direction of extrusion. Manufacturing a metal CAM shaft from metal at Tufts requires either funding for the professional machine shop or additional training in Bray to attempt the process on the CNC mill (a CNC lathe is not available). Practically, a larger CAM shaft and stronger material will address this in a future revision.

Accuracy and precision are critical in the fabrication stage of iterative design. Inconsistencies between the model and physical prototype make it difficult to find what is a design error and what is manufacturing error. Following the first proof of concept design iterations, my concern became identification and resolution of gear skipping and gearbox lock ups. The theoretical accuracy of 3D printed parts using the Prusa i3 research model is 50 microns in the X, Y, and Z directions which should have been sufficient, however this does not consider the cooling shrinkage and warping. I transitioned to laser cut gears and gear rings because the 5.5mm acrylic material deforms less and is faster to fabricate than extrusion of the equivalent parts.

An empirical method was developed to increase the dimensional accuracy of laser cut components. Concentric circles of increasing diameter (20, 25, 30, 35mm…) were modified with increasing tolerances (0.05, 0.10, 0.15mm…) and cut from the material. This procedure allowed me to identify a consistent +0.5mm modification for outer dimensions and -0.2mm modification for inner dimensions with the NOLOP laser.

I tried to cut ring gear from a single piece of 12.80mm thick acrylic in Bray to produce a single component. However, I produced several burned parts and found that the gears did not fit in the undamaged part. This brought my attention to a manufacturing concern with Laser Cutters. I assumed the cut were perpendicular to the surface material, but this is not the case. All components featured a slight draft which is influenced by the angle of the mirror head and the focal point of the laser. As the thickness of the material increases, the draft angle also became steeper. Thus, I resolved to continue using multiple 5.5mm parts.

I returned to the model and examined my assumptions after several unsuccessful laser cut gear iterations. The output shafts of the cycloidal reducer in high-torque reducer designs are also CAM shafts. The absence of eccentric CAM motion at output shaft holes within my gearbox indicated that this was the source of previous gearbox failures. The ratio of the number of tooth lobes and output shaft holes in the gear must be an integer value. In earlier designs, this problem was overlooked because the substitution of 3mm output shafts with M3x25 screws (with a major diameter of 2.9mm) would provide sufficient clearance. Furthermore, I discovered that the output shaft holes must be aligned with the peaks and troughs of the gear lobes. This fault avoided detection because the position of the holes are constrained by the angle with the starting position of the self-intersecting equation-driven spline. As I updated the equation driven spline, the positions of the holes did not update.

Transfer of the design to a final prototype, V6, involves several changes. First, the 2.5x8x5mm bearings on the gears that supported the output shaft were replaced with brass bushings to reduce wear and design complexity. Second, the fixed lobes of the outer gear ring were replaced with 37 shafts and cylindrical rollers to take full advantage of the kinetic friction design. Quick, back of the envelope calculations guided minimum material specifications for the design. During DFM, my colleagues (who have never seen such a design) recommended using steel components in addition for the 6061-T6 aluminum I had specified.

A model for this type of gear that does not depend on equation-driven splines should be developed for future designs. This will support more detailed gear parametrizations and enable the use of finite element analysis to make higher fidelity predictions and reduce reliance on iterative design protocols. Current ideas for V7 revisions, independent of the performance characteristics yet to be evaluated, include the integration of the motor stator into the joint itself to reduce the overall profile of the design and rewinding the motor to produce greater torque with fewer RPM (200kV to 20 to 50 kV). This will allow me to use a smaller gearbox ratio and use a larger CAM shaft. Furthermore, the gearbox was designed to physically limit the rotation beyond the desired range of motion, however rotational limit switches should be integrated as fail safes to prevent the motor driver from increasing the phase current when the motor is stalled at the upper or lower bounds. A limit switch can also participate in the calibration sequence for the rotary encoder.

STRYDSENSE – SUMMARY

The StrydSense surface EMG control system features an Analog Front End sensor and embedded Digital Signal Processing filter cascades. Exoskeleton controls are specific to the application needs, and development of intuitive controls maximizes the utility offered by exoskeletons without detracting from user control over the system.

STRYDSENSE – METHODS

The Analog Front End instrument isolates and amplifies the desired signal spectra. Electromyography depends on the measurement of myoelectric signals produced during the exchange of ions across cellular membranes by muscle activity. The recorded signal, an electromyogram, occupies a signal spectrum of 0-500 Hz and increases intensity as additional muscle fibers are engaged in the flexion activity. The total intensity of the EMG signal is approximately 1-10mV with the most signal rich spectra between 50-150 Hz (Jamal, 2012). An informal relationship between relationship between integrated signal intensity and lifting effort forms the basis of the implemented EMG control technique.

Devices featuring non-invasive designs are preferred over their invasive counter parts where possible because they do not require supervision or training to equip. The placement of surface electrodes is non-trivial because the muscles closest to the detecting surface contribute the most towards the acquired signal, thus contributions from proximal muscle groups can obfuscate the desired muscle signal. Surface EMG electrodes rely on an electrochemical equilibrium between the surface and electrode. Due to the low frequency spectra of the EMG signals, they are susceptible to external noise and artifacts introduced by electrode motion.

The optimal placement of the electrodes depends on the fiber alignment of the muscle group under observation. I selected the flexion of the rectus femourous to the control the hip actuator and the flexion of the biceps femoris to control the knee actuator (Richardson et al., 2012).

There are two classes of surface electrodes: dry and wet electrodes. Dry electrodes are appealing because they do not require a gel electrochemical interface, however these electrodes exhibit capacitive coupling between the user and the sensing interface. This behavior attenuates low frequency signals including the signal spectra of interest and is better suited to higher frequency signals. Wet electrodes, specifically Ag/AgCl electrodes, behave resistively making them more practical for the detection of low frequency signals. In addition to the electrical behavior of the electrodes, the adhesive design of wet electrodes mitigates their migration during use and reduces motion artifacts.

I chose to use an off the shelf bipolar electrode array with differential amplification over the fabrication and assembly of my own design to mitigate errors introduced by the fabrication equipment as well as time and financial concerns. Differential amplification attenuates signals common to both electrodes and reduces the noise introduced by AC power lines at 50 and 60 Hz.

The amplified signal occupies 0 to 3.3V and is quantized by the Analog to Digital converter which exhibits a linear range from 0 to 2.5V based on the internal reference voltage of 2.5V. A sampling frequency of 1000 Hz and bitrate of 12 were selected to satisfy the Nyquist Sampling theorem and to produce manageable data for debugging and design testing.

I used MATLAB to design IIR BiQuad filters with the iirparameq function. IIR filters apply delayed feedback loops to apply attenuation and gain. The absence of clear documentation on how to transfer MATLAB filters to C headers for use in the firmware required research and experimentation. Although I was developing in the STM32CubeIDE environment, I found the ARM Cortex CMSIS DSP library documentation provided by the Keil IDE to be more helpful. It describes the API clearly and provides example code demonstrating the implementation of the functions.

Rather than working directly with ADC samples during the initial design transfer phase, I generated synthetic signals to measure the specific magnitude of attenuation demonstrated by the filter. I designed 50 and 60 Hz power line filters in MATLAB and generated corresponding SOS coefficients to use in the microcontroller code. The frequency response curves for the filters and simulated filtering behavior on synthetic signals in MATLAB demonstrated the desired behavior, however the microcontroller implementation produced unstable filters that produced NaN output after blowing up after several seconds. I continued to implement a 4-band graphic equalizer based on a series of floating-point digital filters. Each band features 19 filters that represent every gain for the frequency band between -9 and 9 dB. Because the firmware implementation was correct, but the behavior was wrong it became a matter of identifying the error in design transfer between the MATLAB and CMSIS API.

I compared the CMSIS DSP API as described in the Keil documentation and the output generated by the MATLAB iirparameq function. The format of the SOS coefficients generated by MATLAB were different because the transfer function was written differently:

	Transfer Function	SOS Array Format
MATLAB SOS	$H(z)=\prod_{k=1}^{L}\frac{b_{0k}+b_{1k}z^{-1}+b_{2k}z^{-2}}{a_0+a_{1k}z^{-1}+a_{2k}z^{-2}}$	[b0 b1 b2 a0 -a1 -a2] $a0 \equiv 1$
ARM CMSIS DSP API	$H(z)=\prod_{k=1}^{L}\frac{b_{0k}+b_{1k}z^{-1}+b_{2k}z^{-2}}{1+a_{1k}z^{-1}+a_{2k}z^{-2}}$	[b0 b1 b2 a1 a2]

Table 3.0 Initial difference in SOS Array format

This error was self-evident as the size of the array was incorrect. Correcting the output array to exclude the column from the array corrected the shape of the filter but did not address the gain/attenuation. SOS and SV variables are created by the MATLAB iirparameq function and when the SV variable was excluded from the visualization, the MATLAB and microcontroller output became more similar.

The gain is only applied to the numerators of the transfer function, however the SV array contained an additional value, making vector multiplication impossible. I deleted the last coefficient in the SV array and multiplied the values stored in the SV gain vector by the SOS coefficient numerators [b0,b1,b2]. I tried this because I removed the a0 value from the array and it seemed that the value would correspond a0. The correct representation of the transfer function:

$$H(z)=\mathrm{SV}\prod_{k=1}^{L}\frac{b_{0k}+b_{1k}z^{-1}+b_{2k}z^{-2}}{a_0+a_{1k}z^{-1}+a_{2k}z^{-2}}$$

This reduced the errors between MatLab and microcontroller execution to 10^{-6} and 10^{-24} which can be attributed to computational errors associated with the use of Direct Transform II form filters with floating point numbers.

I reviewed and compared filter performance by manually exporting ADC samples and output data with a memory explorer. This is a tedious and labor-intensive method of accessing data stored in the memory. After struggling to implement a Arduino based USB UART solution, I discovered that my developer board (DISC1) supported UART over USB.

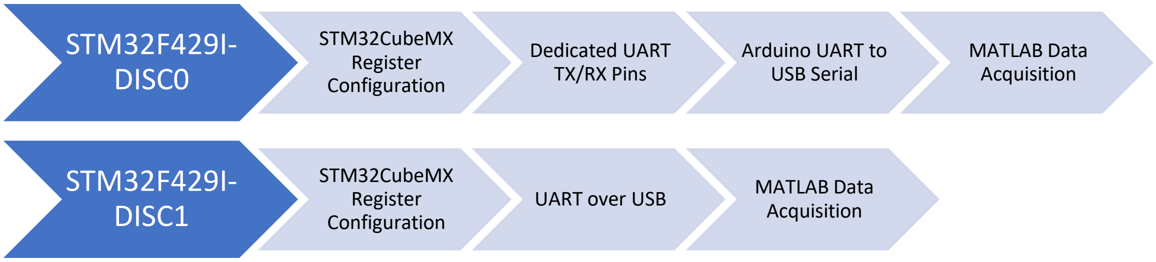

I restored the pinout of the project prior to the attempted Arduino solution and configured the virtual serial COM port in the STM32CubeMX program. The ADC input and filtered output data streamed as ordered pairs to my MATLAB session for visualization, thus accelerating the debugging process.

STRYDSENSE – RESULTS

Figure 6 depicts the frequency responses of the 50 and 60 Hz power line filters as well as the 76 separate filters used in the graphic equalizer. These filters perform the attenuation of power line noise and provide an adjustable gain for 0-20 Hz noise introduced by electrode motion, 20-65 Hz signals associated with low frequency EMG signals, 65-165 Hz signals within the EMG rich spectra, and 165-500 Hz signals associated with high frequency signals and noise. These will be used to amplify signals in weaker muscles and attenuate cross talk introduced by muscles close to the sensor.

Figure 8.0 compares the ADC input and filtered output of the DSP system. Equalizer gain was set to 0 dB across all bands for this graphic. Time based distortion in the filtered output signal is associated with the uncorrected group delays introduced by the IIR BiQuad filters.

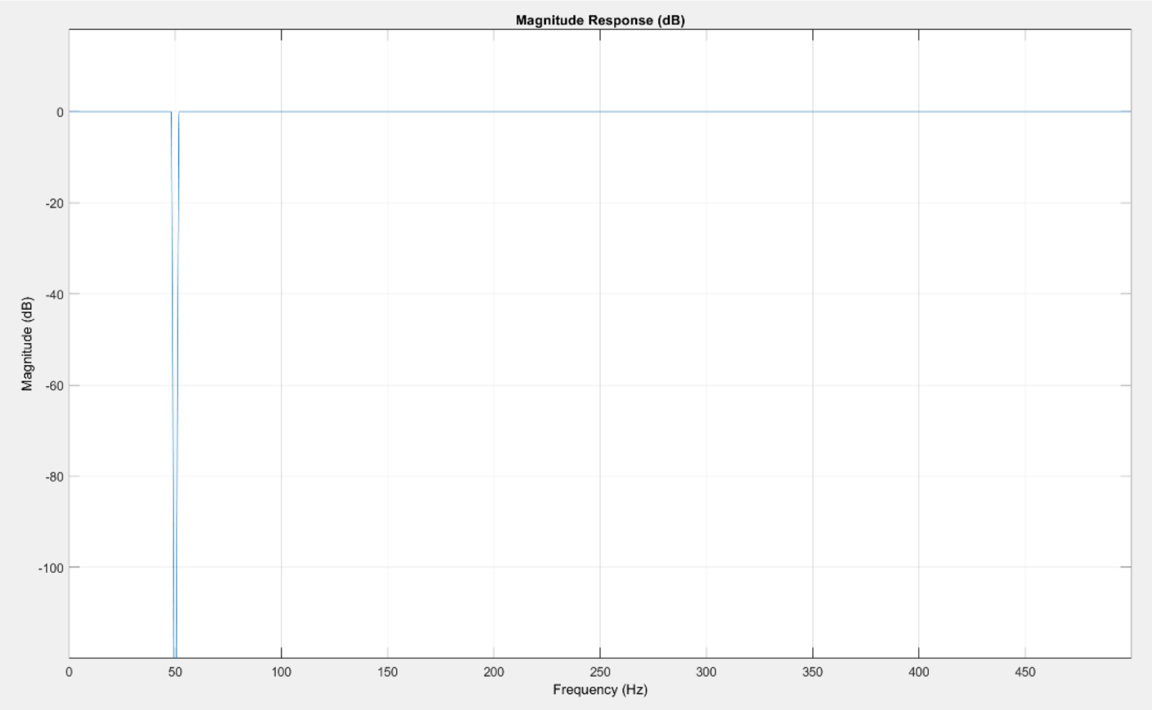

Figure 7.a
10th Order IIR BiQuad
50 Hz Powerline Filter

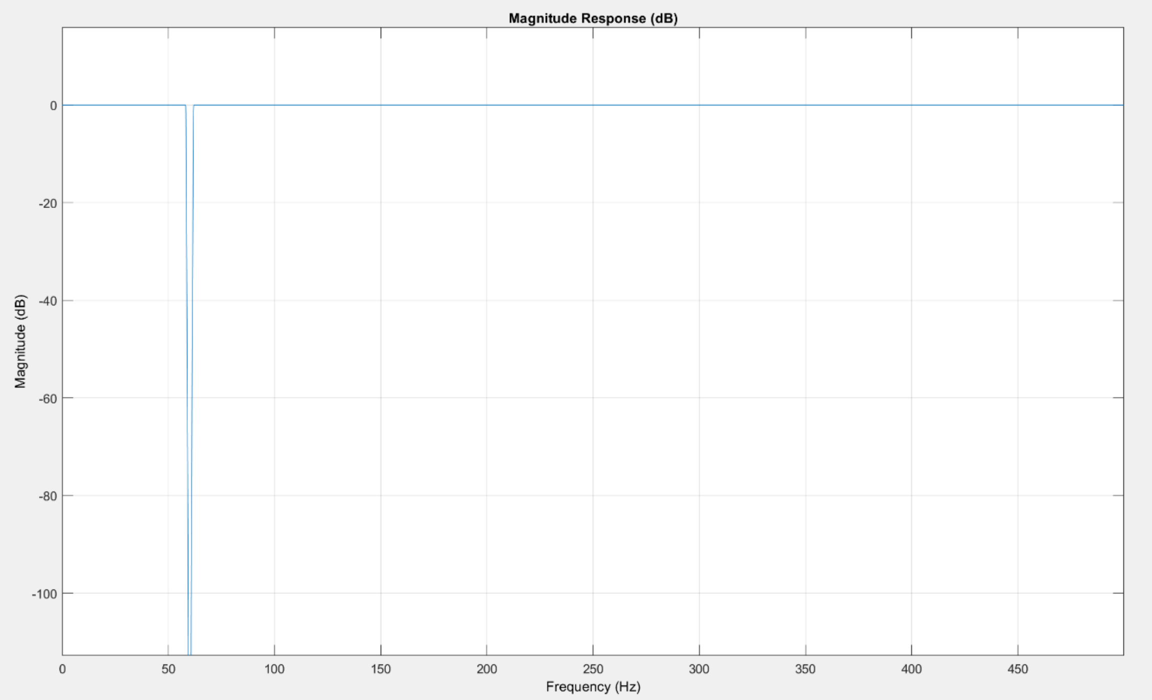

Figure 7.b
10th Order IIR BiQuad
60 Hz Powerline Filter

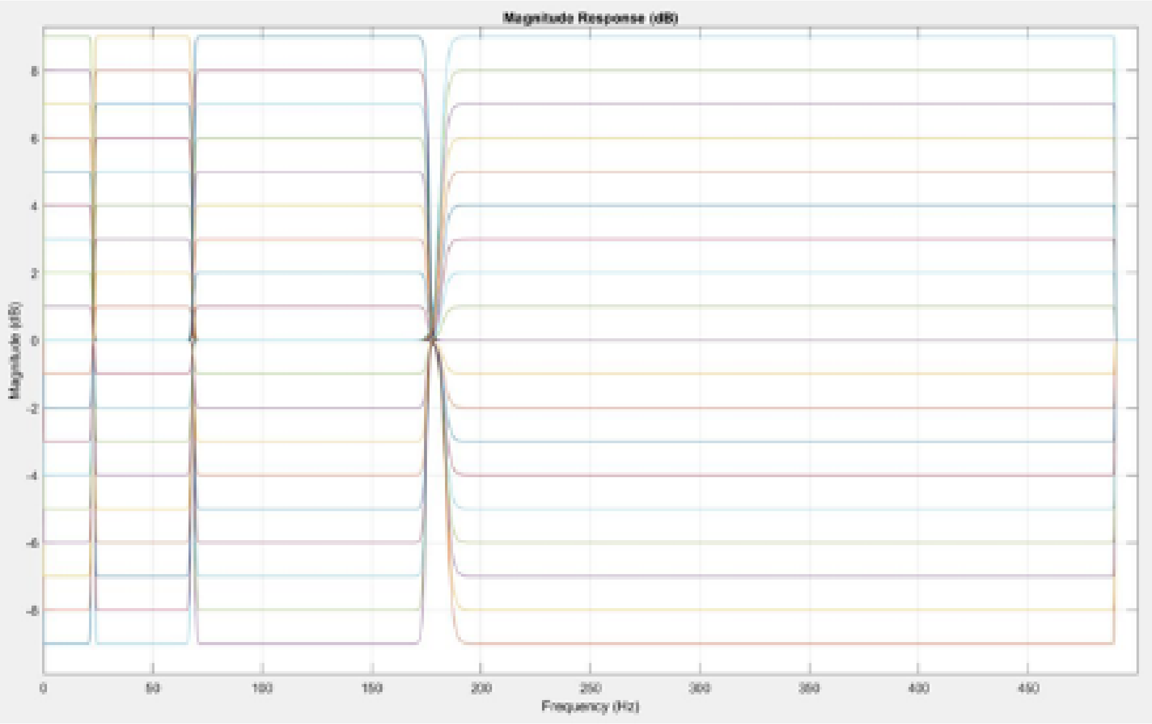

Figure 7.c
100th Order IIR BiQuad 4 Band Equalizer with 19 Filters per Band (-9dB …. 0 dB …. +9dB)

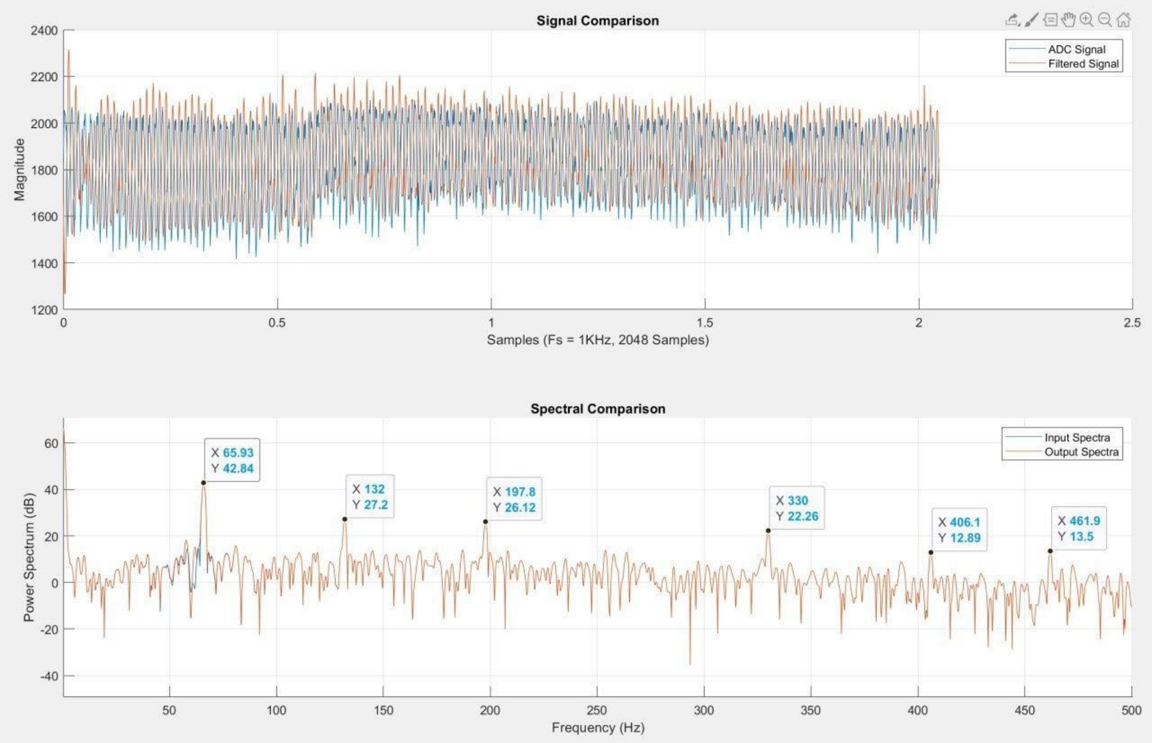

Figure 8.0
STM32 ADC input compared with filtered output. Equalizer gain set to [0,0,0,0] dB and 60 Hz powerline filter attenuation is visible in the Spectral Comparison plot (bottom). Time shifts introduced by BiQuad filtering group delays are visible in time based spectrum (top).

STRYDSENSE – DISCUSSION

The bipolar electrode circuit features an electrode separation of approximately 3 cm which is larger than I would like to use because the increased distance introduces additional crosstalk (Jamal, 2012). I placed the sensor between the muscle and musculotendinous junction along the midline of the muscle. Signal conduction is poor when the electrodes are placed too close the tendon or too far to the sides, so this requires some practice, trial, and error.

The digital processing of the EMG signals involves the quantization of the analog, continuous time signal into discrete valued, discrete time signals. The conversion is performed by an Analog to Digital Converter (ADC) which quantizes the data at timed intervals. I began project development on the Texas Instruments MSP430G2553 microcontroller and quickly ran into problems. The ADC on this particular microcontroller was limited a maximum sampling resolution of 10-bit and rate of 125kHz. Furthermore, the configuration of the ADC to use the internal reference voltage of (2.5V) to ensure accurate signal sampling had the unintended consequence of limiting the viable 10-bit sampling range (1024 discrete values over 0-3.3V) to 775 different values over 0-2.5V. Furthermore, the Texas Instruments MSP-DSP library produced fixed point filters rather than floating point filters adding an additional layer of quantization to the data processing and introduce potential sources of error. This particular chip, while supported by the library, did not include some of the hardware accelerated functions. The filtering system developed with the Texas Instruments MSP-DSP library quickly consumed the RAM.

I upgraded within the same family to the MSP430FR5994, the chip for which the DSP library was designed, to gain access to the 12-bit ADC which I configured to run at 1000 Hz to satisfy the Nyquist sampling theorem. Although I was still limited by the 2.5v internal reference voltage, I had increased the linear resolution from 775 values to 3,103. I became aware of inconsistent sampling rates and filter output errors between the chips. The sampling discrepancies were not systemic which eliminated the possibility of quantization errors. I came to suspect clock stability when the error margin continued to grow with extended power on time. The chips were not sufficiently warm to be experiencing thermal throttling, so I looked at the data sheets for the processors themselves.

The clock speed of microcontrollers is established by the ringing of a crystal oscillator. The Texas Instruments MSP430 development kits relies exclusively on an internal crystal for development and debugging. This crystal is affected by operating temperature and has a 6% instability in clock speed. The ADC and all peripherals on the system bus were affected by the clock instability. The most immediate effect of this is on the 1000 Hz sampling rate of the ADC, which was fluctuating between 940 and 1060 Hz. Two possible solutions are possible – continued development with the MSP430 family by designing, assembling, and integrating an external crystal oscillator to the system or to continue development a better platform all together.

I transitioned from the 16 MHz Texas Instruments MSP430 microcontroller family to the 180 MHz STMicroelectronics STM32F429I-DISC1 development kit. The processor features an external crystal with a Phase Lock Loop (PLL) that uses a feedback loop to ensure clock speed stability. In addition to the superior development kit design, the ARM Cortex-M4 processor is a giant leap in system architecture and includes 16-bit ADCs/DACs and two Direct Memory Access controllers. I intended initially to rely heavily on the MATLAB Simulink embedded coder software plug-in to develop firmware for the device. However, I found myself struggling to correctly configure the registers control the behavior of the microcontrollers through the Simulink Interface.

I began to configure the registers using the STM32CubeMX software and develop firmware for the microcontroller with the STM32CubeIDE. To take advantage of the hardware accelerated digital signal processing functions, I had to familiarize myself with the Cortex-M4 microcontroller Software Interface Standard (CMSIS) which is a hardware abstraction layer for ARM Cortex processors to circumvent vendor-specific code. I familiarized myself with the CMSIS DSP codebase with the Keil IDE documentation. I was able to recreate example code demonstrating the use of the filter and believed that I could complete the design this way.

I designed my Second-Order Section BiQuad filters in Transposed Direct form II. A complete discussion of the benefits associated with each form are beyond the scope of this work, however a transition to Transposed Direct Form I is recommended in future work. The accuracy of floating-point filters is improved when intermediate sums are closer in value because the addition of floating-point numbers with large differences is less precise.

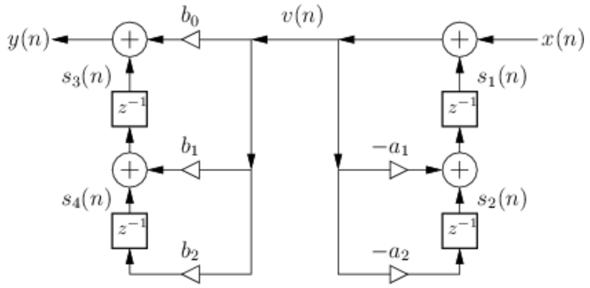

Figure 9.a
Transposed Direct Form I (Smith, 2008)

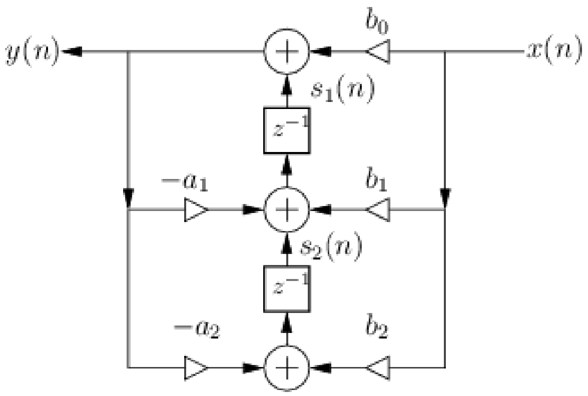

Figure 9.b
Transposed Direct form II (Smith, 2008)

Development of firmware with optimized CPU usage and filter corrections was delayed due to limitations introduced by the COVID-19 pandemic. Features like Direct Memory Access, Zero-Phase filtering, and duty cycling ramping will be implemented at a later date.

The STM32F429 features two dedicated DMA controllers (Direct Memory Access) which are sectors of silicon dedicated to taking control of the system bus and facilitating data transfer from peripheral interfaces like the ADC to memory without relying on the CPU. When correctly implemented, data sampled from the ADC can be recorded into a buffer which is transferred directly to the microcontroller's memory without interrupting the CPU's current task (filtering). There are several modes to choose from depending on the peripheral and data transfer needs. Based on the desire for reduced latency, "direct" transfers from the ADC to RAM make sense. A circular buffer of double length is simultaneously accessed by the CPU and DMA controller. Separate pointers indicate the starting position of each region of the buffer and are swapped when the DMA fills a buffer. The DMA interrupt for completing a transfer will initiate CPU filtering on the newly filled region of the buffer while the DMA controller continues to transfers data to the region that occupied input values that have already been filtered. This is exceptionally memory and CPU efficient and circumvents the need for task threading.

Group delays are a side effect of feedback-based filtering. This phenomenon is the result of time delays associated with signals of specific frequencies passing through filter faster or slower than others, producing time shifted output. The way to correct this problem is to reverse the filtered signal and pass it through the filter again. This has the effect of applying the specified gain or attenuation a second time and “undoes” the original phase shift. This method, referred to as Zero-Phase filtering, is actually implemented in a commonly used MATLAB filtfilt function. Signals processed in this manner will be in phase with the source signal and only require a filter of half the original order. This reduces the total number of hard-coded coefficients stored in the flash and reducing access and processing time.

The integrated intensity value filtered by StrydSense will be used calculated a ramped signal for the oDrive controller used in the StryDrive. The PWM ramping will smooth the motor acceleration to provide more comfortable joint motion.

STRYDLIGHT – SUMMARY

The StryLight carbon-fiber composite frame provides equivalent strength with less inertial mass. This reduces user fatigue and the energy and performance impact of applying opposing torque during an actuator direction change. StrydLight also encompasses the interfaces between the user's body and frame as well as the passive, load-bearing ankle that transmits the weight and load carried by the exoskeleton to the ground.

STRYDLIGHT – METHODS

StrydLight provides structural support between the components of the exoskeleton as well as a comfortable interface with the user. The selection of cylindrical carbon-fiber tubes was influenced by financial limitations and personal experience accommodating rectangular extrusions. Hobby grade carbon-fiber components used in custom drones are less expensive and less reliable than reputably sourced and certified carbon-fiber structural elements. However, for the purposes of a proof of concept design, replacements can always be made until such a time where premium components can be sourced. Rectangular tubes provide superior rigidity due to their area moment of inertia but are more difficult to develop systems around because compensating for tolerances in multifaceted geometry is more difficult (see appendix).

The condition and tolerances of composite parts can pose design liabilities and are identified during inventory inspection prior to use. The fiber reinforced epoxy can develop stress concentrations along damaged fiber strands, making them more prone to sudden fracture and failure (see Figure 10). Although I did not find any defects, the practice is key to preventing unexpected and hazardous failures. Each structural element was tagged and measured. Components in StrydLight were designed around the tolerances measured here to minimize the use of tape to compensate for defects (see Table 4.0).

Working with composite materials poses a potential health hazard during cutting operations. The release of fine carbon-fiber shrapnel and epoxy dust requires a well-ventilated workspace with personal protective equipment for skin, eyes, and lungs as well as a HEPA filter equipped vacuum cleaner. If the vacuum cleaner does not feature such a filter or insulation over the motor or driver circuit, it will be damaged as it aerosolizes the fine dust.

The use of hollow structural elements as conduit for cabling requires preparation because carbon-fiber is conductive and requires insulation to prevent the transmission of potentially hazardous shock. Meeting the Society of Automotive Engineering requirements for restrict the use of composites is beyond the scope of this project. Furthermore, increasing the distance between the motor and current sensing circuit increase the measured phase resistance of the motor which affects the accuracy of the Field-Oriented Control algorithm used for motor commutation. A new motor controller would need to be designed and that is also beyond the scope of this project.

I used a cantilever inspired clamp for the body interfaces and telescoping system (see Figure 11). It is difficult to accurately calculate the required length and thickness of the beams. This is because the part, while designed as solid components in Solidworks, are reprocessed into semi-hollow models during the 3D printing process. Compensation for the changes introduced by the printer slicing software would require a system to recreate a solid body from GCode on which FEA could be performed.

The need to quickly and easily equip or unequip the exoskeleton is a necessity defined early in the project. Nylon straps secure an FDM 3D printed brace against the pilots' leg with a machine washable, nylon pad and a Fiddlelock brand clasp. The carbon fiber reinforced nylon clasp is magnetically aligned so that it can be easily mated from multiple approach vectors with minimal coordination and can only be separated by pulling or pushing it in a single direction. This provides a friendly and accessible latching experience with the security of less friendly latches.

Loads carried by the exoskeleton frame must be transferred to the ground to minimize discomfort to the user. There are many examples of ankle-based exoskeletons and augmentation systems that show promise in improved running and jumping efficiency. However, these benefits would be lost in lifting exercises. A passive, 2-degree of freedom ankle was designed to promote the normal range of motion and prevent over extension.

STRYDLIGHT – RESULTS

StrydLight was the most impacted by COVID-19 as development and testing were suspended shortly after development resumed in the Spring term. Limited qualitative testing of the ankle's range of motion during unassisted walking and stair climbing activities were completed. Testing was limited to smooth, flat surfaces.

STRYDLIGHT – DISCUSSION

Although the system meets the minimum requirements for overall system testing, it did not have the opportunity to mature. Further development is required before testing can occur.

The use of mass-produced, hobby grade carbon fiber cylindrical tubes demonstrate the weight savings and provide structural support. The true loading capacity of these hobby grade tubes is unverified and would require additional material testing beyond the scope of this project. Structural rigidity can be improved with a rectangular cross-sectional area; however, the design of telescoping components and body interfaces would have become required higher precision components to circumvent compatibility problems.

The cantilever clamp and tool-free handle design pose a problem. Because the iteratively design components were printed from PLA plastic and feature a percentage infill rather than solid mass, simulations of the stiffness and clamping force were meaningless. Designing this component from aluminum would be more practical and shall be included in the scope of the next revision to use rectangular frames.

The plastic, tube-mounted interfaces between the frame and the user are comfortable for short term use. Despite the use of soft nylon sleeving and foam padding, the strap and body interface is not as comfortable as it could be.

The passive ankle provides load-bearing support and does not impede my range of motion. However, the lack of a return to center behavior makes it a tripping hazard for individuals who cannot fully lift the foot. Passive solutions based on springs, spring steel, and hydraulics are just too complicated for what this needs to be. A rubber polyurethane bushing should provide the necessary rebound and can be tailored with different durometer versions of the same part. Finally, a shoe platform must be designed to substitute the a failed 3D print I repurposed as a platform.

Front End Measurements in mm (5x)							Rear End Measurements in mm (5x)						
Tag	#1	#2	#3	#4	#5	Average	Tag	#1	#2	#3	#4	#5	Average
A	30.22	30.08	30.23	30.12	30.19	30.168	A	30.16	30.12	30.12	30.19	30.12	30.142
B	30.05	30.24	30.2	30.05	30.21	30.15	B	29.92	30.03	29.83	30.01	29.82	29.922
C	30.07	30.11	30.13	29.95	30.07	30.066	C	30.12	30.02	30.14	30.08	30.11	30.094
D	30.23	30.13	30.23	30.15	30.30	30.208	D	29.98	30.08	30.02	29.94	30.03	30.01
E	30.33	30.16	30.15	30.15	30.12	30.182	E	30.11	29.96	30.10	29.95	30.08	30.04
F	30.05	30.00	30.04	30.00	30.04	30.026	F	29.86	29.94	29.92	29.97	29.95	29.928
G	30.08	30.00	30.05	30.04	30.02	30.038	G	30.22	30.08	30.03	30.08	30.01	30.084
H	30.04	30.10	30.05	30.09	30.09	30.074	H	30.04	30.23	30.04	30.13	30.09	30.106
					Average	30.114						Average	30.041
					Max	30.208						Max	30.142
					Min	30.026						Min	29.922
					Diff	0.094						Diff	0.119

Table 4.0 Inventory measurements of 3K carbon-fiber circular tubes ($\emptyset_{OD} = 30mm, \emptyset_{ID} = 28mm, L = 500mm$)

Figure 10.0
Inspection of the carbon fiber structural elements.

Figure 11.a
Cantilever style clamp for body interface mount.

Figure 11.b
Cantilever style clamp for telescoping frame design

Figure 11.0
V2 knee to ankle frame assembly with StryDrive

CONCLUSIONS

The Strydr exoskeleton was partially successful in the ambitious design and testing of the StryDrive, StrydSense, and StrydLight subsystems.

I successfully parameterized and qualitatively tested a cycloidal reducer, designed an in-joint actuator, and drafted design documents. However, manufacturing and quantitative characterization of the cycloidal reducer through static and cyclic loading tests are incomplete due to COVID-19 and will not occur prior to the final submission of the project.

I successfully designed digital filters and implemented the core signal acquisition and hardware accelerated processing techniques required for SEMG controls. However, implementation and testing of simultaneous sampling and processing, zero-phase filtering, and control signal ramping are incomplete due to COVID-19 and will not occur prior to the final submission of this project.

I successfully designed and qualitatively tested a telescoping frame, user interface, and passive ankle design. However, the design and testing of passive return to center behavior of the ankle joint, an easily equipped shoe platform, and tool-free handle for cantilever style clamps are incomplete due to COVID-19 and will not occur prior to the final submission of this project

Future work must complete the Strydr exoskeleton before characterization can occur.

ACKNOWLEDGMENTS

I would like to thank my uncle, Frederick Meyerson J.D. Ph.D., for providing a lot of emotional support throughout this difficult time and enforcing a minimum exercise routine during the final days as a Tufts undergraduate. I would like to thank the staff at ProjX (China) for helping me machine components.

REFERENCES

ams AG. (2016). *AMS AS5047P Rotary Encoder Datasheet*. https://ams.com/documents/20143/36005/AS5047P_DS000324_2-00.pdf

Bogue, R. (2015). Robotic exoskeletons: A review of recent progress. *The Industrial Robot; Bedford*, *42*(1), 5–10. http://dx.doi.org.ezproxy.library.tufts.edu/10.1108/IR-08-2014-0379

Borislavov, B., Borisov, I., & Panchev, V. (2012). *Design of a Planetary-Cyclo-Drive Speed Reducer: Cycloid Stage, Geometry, Element Analyses*. Linnaeus University, School of Engineering.

Bureau of Labor Statistics. (2019). *Employer-Reported Workplace Injuries and Illnesses-2018* (p. 8) [News Release]. https://www.bls.gov/news.release/pdf/osh.pdf

Compact Mechatronic Drive for Robotic Applications | RoboticsTomorrow. (n.d.). Retrieved November 13, 2019, from https://roboticstomorrow.com/article/2019/05/compact-mechatronic-drive-for-robotic-applications/13676

Fagan, K. M., & Hodgson, M. J. (2017). Under-recording of work-related injuries and illnesses: An OSHA priority. *Journal of Safety Research*, *60*, 79–83. https://doi.org/10.1016/j.jsr.2016.12.002

Greenbaum, D. (2016). Ethical, legal and social concerns relating to exoskeletons. *ACM SIGCAS Computers and Society*, *45*(3), 234–239. https://doi.org/10.1145/2874239.2874272

Gregorczyk, K. N., Hasselquist, L., Schiffman, J. M., Bensel, C. K., Obusek, J. P., & Gutekunst, D. J. (2010). Effects of a lower-body exoskeleton device on metabolic cost and gait biomechanics during load carriage. *Ergonomics*, *53*(10), 1263–1275. https://doi.org/10.1080/00140139.2010.512982

Herr, H. (2009). Exoskeletons and orthoses: Classification, design challenges and future directions. *Journal of NeuroEngineering and Rehabilitation*, *6*(1), 21. https://doi.org/10.1186/1743-0003-6-21

Jamal, M. Z. (2012). Signal Acquisition Using Surface EMG and Circuit Design Considerations for Robotic Prosthesis. *Computational Intelligence in Electromyography Analysis - A Perspective on Current Applications and Future Challenges*. https://doi.org/10.5772/52556

Li-aung Yip. (2013, December 6). Answer to Question “Three phase power supply—What is line to line voltage” [Stack Exchange]. *ElectricalEngineering Stack Exchange*. https://electronics.stackexchange.com/a/92826

Masood, J., Ortiz, J., Fernández, J., Mateos, L. A., & Caldwell, D. G. (2016). Mechanical design and analysis of light weight hip joint Parallel Elastic Actuator for industrial exoskeleton. *2016 6th IEEE International Conference on Biomedical Robotics and Biomechatronics (BioRob)*, 631–636. https://doi.org/10.1109/BIOROB.2016.7523696

Minchala, L. I., Velasco, A. J., Blandin, J. M., Astudillo-Salinas, F., & Vazquez-Rodas, A. (2019). Low Cost Lower Limb Exoskeleton for Assisting Gait Rehabilitation: Design and Evaluation. *Proceedings of the 2019 3rd International Conference on Automation, Control and Robots*, 55–60. https://doi.org/10.1145/3365265.3365276

Molteni, F., Gasperini, G., Cannaviello, G., & Guanziroli, E. (2018). Exoskeleton and End-Effector Robots for Upper and Lower Limbs Rehabilitation: Narrative Review. *PM&R*, *10*(9S2), S174–S188. https://doi.org/10.1016/j.pmrj.2018.06.005

Mosher, R. S. (1967). *Handyman to Hardiman*. 670088. https://doi.org/10.4271/670088

National SCI Statistical Center. (2017). *Spinal Cord Injury Facts and Figures at a Glance*.

Ohm, D. Y. *DYNAMIC MODEL OF PM SYNCHRONOUS MOTORS*. 10.

Ohm—DYNAMIC MODEL OF PM SYNCHRONOUS MOTORS.pdf. (n.d.). Retrieved May 4, 2020, from https://pdfs.semanticscholar.org/e2be/948549aaf744c73b36d303cf7165041222f4.pdf

Pirker, W., & Katzenschlager, R. (2017). Gait disorders in adults and the elderly. *Wiener Klinische Wochenschrift*, *129*(3), 81–95. https://doi.org/10.1007/s00508-016-1096-4

Proakis, J. G., & Manolakis, D. G. (2007). *Digital signal processing: Principle, algorithms, and applications*. Pearson Prentice Hall.

Repperger, D. W., Remis, S. J., & Merrill, G. (1990). Performance measures of teleoperation using an exoskeleton device. , *IEEE International Conference on Robotics and Automation Proceedings*, 552–557 vol.1. https://doi.org/10.1109/ROBOT.1990.126038

Richardson, P., Drake, R. L., Horn, A., Tibbitts, R., Mitchell, A. W. M., & Vogl, W. (2012). *Gray's Basic Anatomy*. Elsevier Health Sciences.

Rupal, B. S., Rafique, S., Singla, A., Singla, E., Isaksson, M., & Virk, G. S. (2017). Lower-limb exoskeletons: Research trends and regulatory guidelines in medical and non-medical applications. *International Journal of Advanced Robotic Systems*, *14*(6), 172988141774355. https://doi.org/10.1177/1729881417743554

Sanchez-Villamañan, M. del C., Gonzalez-Vargas, J., Torricelli, D., Moreno, J. C., & Pons, J. L. (2019). Compliant lower limb exoskeletons: A comprehensive review on mechanical design principles. *Journal of NeuroEngineering and Rehabilitation*, *16*. https://doi.org/10.1186/s12984-019-0517-9

Soucie, J. M., Wang, C., Forsyth, A., Funk, S., Denny, M., Roach, K. E., Boone, D., & THE HEMOPHILIA TREATMENT CENTER NETWORK. (2011). Range of motion measurements: Reference values and a database for comparison studies: NORMAL JOINT RANGE OF MOTION. *Haemophilia*, *17*(3), 500–507. https://doi.org/10.1111/j.1365-2516.2010.02399.x

Thorson, I., & Caldwell, D. (2011). A nonlinear series elastic actuator for highly dynamic motions. *2011 IEEE/RSJ International Conference on Intelligent Robots and Systems*, 390–394. https://doi.org/10.1109/IROS.2011.6094913

US420179. (n.d.). Retrieved October 27, 2019, from https://patentimages.storage.googleapis.com/0f/e0/2c/161bea0a876b81/US420179.pdf

US440684. (n.d.). Retrieved October 27, 2019, from https://patentimages.storage.googleapis.com/94/70/4e/f46773a82b1caa/US440684.pdf

Zhang, X., Yue, Z., & Wang, J. (2017). Robotics in Lower-Limb Rehabilitation after Stroke. *Behavioural Neurology*, *2017*. https://doi.org/10.1155/2017/3731802

APPENDICES

DT4020 Brushless DC Motors

The motor herein described is not available for consumer purchase and is produced in limited quantities at the discretion of the manufacturer, SunRay Technology Co., Ltd. Shenzhen in association with ProjX (China).

Property	Value
Stator Diameter	⌀40 [mm]
Stator Height	20[mm] Total, 0.35 [mm] Laminations
Slot/Pole Ratio	10/14
Magnet	N33SH Radial (Max 150 °C)
Winding	200 [Kv]
Maximum Torque	3 [Nm] (72 Amp DC Phase Current)

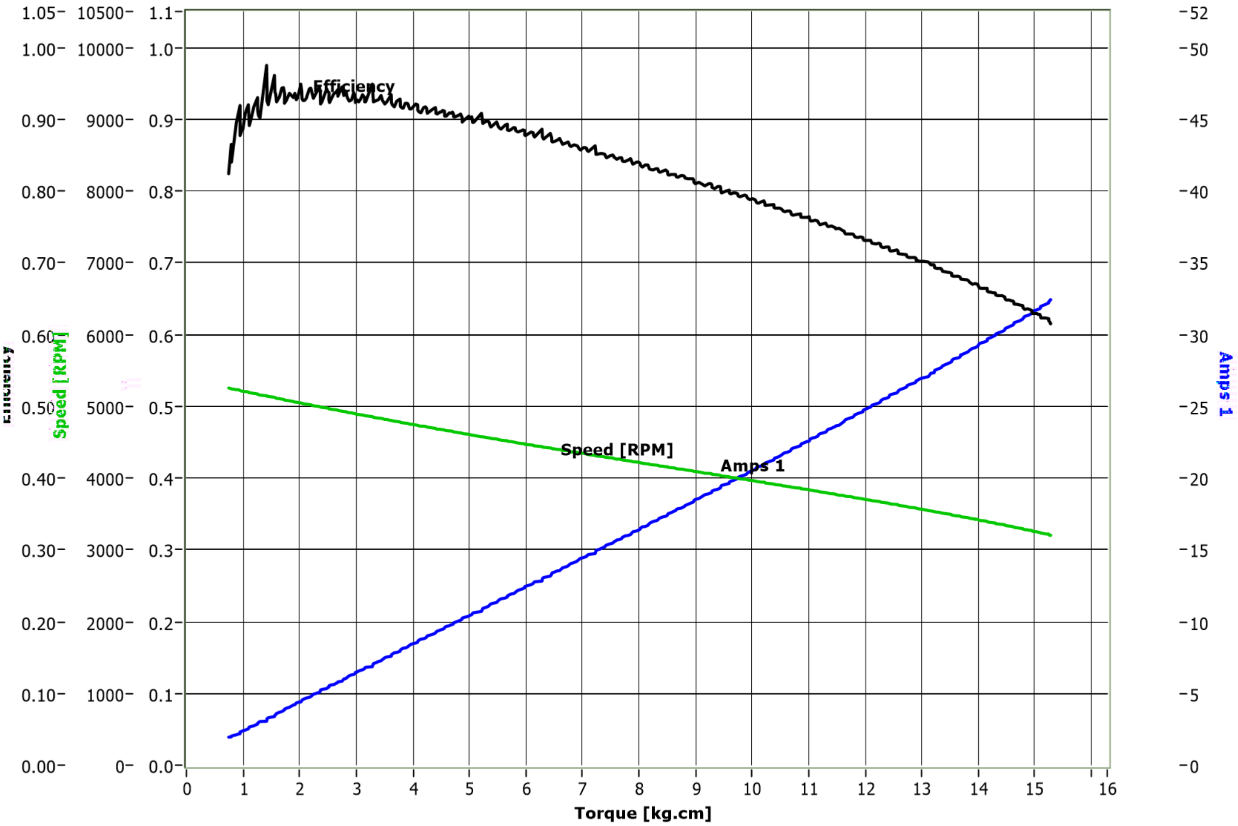

Dynamo testing of the motor at 25.8V DC using BLDC commutation

BLDC/PMSM Motor Theory

Brushless DC motors and permanent magnet synchronous motors are both synchronous motors with permanent magnets attached on their rotors, however the counter-electromotive waveform of PMSM motors is trapezoidal whereas Brushless motors exhibit sinusoidal CEMF waveforms.

Brushless DC Motors are rated by the constant velocity per volt, Kv. The motor specified in the project is rated at 200 Kv. The counter-electromotive force generated by 200 revolutions per minute 1 Minute is a 1 volt. The torque constant, Kt, is often misrepresented as the reciprocal of Kv. The true expression is closer to:

$$Kt \ = \left(\frac{1}{Kv}\right)\left(\frac{3}{2}\right)\left(\frac{1}{\sqrt{3}}\right)\left(\frac{60}{2\pi}\right)$$

These modifications take into account the synchronous inductance (Ohm), conversion of line to line voltage to represent the phase voltage (Li-aung Yip, 2013), and the conversion from RPM to Rads/s. The Kt of a 200 Kv motor is approximately 0.04135 $\left(\frac{Nm}{A}\right)$

The generated torque (Nm) is the product of the instantaneous phase current and Kt constant. An accurately estimate of the phase current required to generate 3 Nm can be found by rearranging this expression:

$$I \ = \frac{3[Nm]}{0.04135 \ \left[\frac{Nm}{A}\right]} \ = \ 72.55 \ Amps$$

Phase current is NOT the same as supply current. However, this phase current is pushing the upper limits of the motor phase insulation rating and should not be used continuously.

Brushless DC Motor Commutation Theory

A brushless DC motor controller is switching the current flow through an inductive load (the motor) with a multi-phase bridge structure. Regardless of the winding scheme of the motor, transistor gates open and close briefly exposing the DC power supply to the motor and the Motor's CEMF to the power supply. Conceptually, the DC bus, transistor and diodes, inductive load, and generated BEMF create a DC/DC Buck Converter.

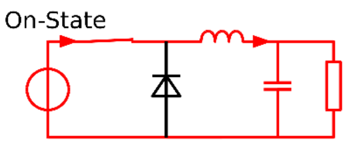

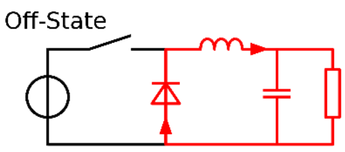

DC/DC Buck Converters exploit the induced potential developed by the flow of current through an inductor. Procedurally,

1. Current flows through inductor initiating voltage drop across inductor due to changing current storing power in magnetic field.

2. Current flow is reduced, thus decreasing the magnetic field and initiating a voltage drop across the conductor.
3. The inductor becomes a current source because of the power stored in the magnetic field.

The potential and current that can be extracted from the magnetic field depend on the inductors geometry (or losses associated with motion). The conservation of energy can be summarized as:

$$P_{in} = P_{out} + P_{Losses}$$

$$P_{in} = V_{Supply} * I_{Supply}$$

$$P_{out} = V_{CEMF} * I_{Phase}$$

Field Oriented Control Theory

This motor commutation method observes the current flow through motor phases to isolate radial pulling force (I_D) from tangential torque (I_Q). Minimizing the current flow associated with radial pulling reduces vibrations, thereby producing smoother, quieter, and cooler torque compared with typical BLDC commutation algorithms that do not distinguish or optimize the current flow to maximize torque. Measurement of resistive and inductive properties of the motor is performed using the existing phase current sensing shunts and is required to calculate the vectors.

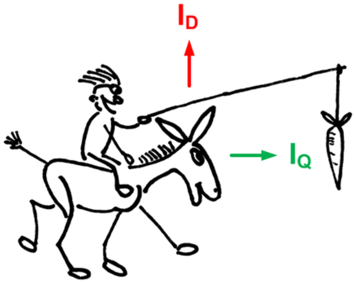

Graphic borrowed from TRINAMIC

https://www.trinamic.com/technology/std-technologies/field-oriented-control/

Gearbox Reduction Calculation

The desired torque of 100 [Nm] and maximum motor output of 3 [Nm]: $\frac{100}{3} = 33$

To include some wiggle room, the selected reduction ratio is 36. The value of N_{Gear} and N_{Ring} is found with the expression for the cycloidal reducer ratio, i:

$$36 = \frac{36}{37 - 36}$$

Mechanical and electrical torque losses are estimated at 0% (perfectly efficient), 10%, and 20%:

$$Torque_{Final} = Torque_{Input} * Ratio * Efficiency$$

% Inefficiency	Torque Production
0%	108 [Nm]
10%	97.2 [Nm]
20%	86.4 [Nm]

MATLAB SOS Coefficients to C header Code

```
% Verify that the filter is stable before transforming.
% Filter_Object contains the SOS and SV arrays which are the
% output of the biquad filter generating function.

if (isstable(Filter_Object))
     % Modify the Second-Order Section data
          % Eliminate Extraneous a0 value from array
          SOS = SOS(:,[1 2 3 5 6]);
          % Correct Sign of the SOS denominator (a1,a2)
          SOS = SOS.*[1 1 1 -1 -1];
     % Apply Gain Value to numerator (b0,b1,b2)
          % Remove extraneous gain value
          SV = SV(1:end-1);
          % Apply SV to Numerators
          Coeffs=[SOS(:,1:3).*SV SOS(:,4:5)];;
end
```

Gearbox Stress Estimates and Material Selection

Due to limitations in the Solidworks model, I am performed a quick estimate of the stresses within the gearbox to guide the selection of the gearbox materials.

The 3Nm BLDC motor with a 36:1 gearbox with efficiency of 92% produces about 100Nm of torque. Assuming (incorrectly, but conservatively) that all of the load is applied to ONE tooth at a radius of 35mm, a force of $0.035[m] * 100[Nm] = 3.5[N]$ would be distributed across 20% of the circumference of a 4mm OD, 5mm tall contact patch.

$$Area = 5 * \left(0.2 * \left(2 * \left(\frac{4}{2}\right) * \pi\right)\right) \approx 12.5[mm^2]$$

The expected stress is $\frac{3.5[N]}{12.5\ [mm^2]} = 0.28\ MPa$ which is very low compared to the yield stress of the 6061-T6 aluminum and should deform negligibly.

Structural Element Buckling and Bending

I apologize, this appendix may not be completed before the deadline.